An Inverse Thermogelling Bioink based on an ABA type Poly(2-oxazoline) Amphiphile

Lukas Hahn[1], Emine Karakaya[2], Theresa Zorn[3], Benedikt Sochor[4], Matthias Maier[1], Philipp Stahlhut[5], Stefan Forster[1], Karl Fischer[6], Sebastian Seiffert[6], Ann-Christin Pöppler[3], Rainer Detsch[2] and Robert Luxenhofer[1,7]

[1]*Functional Polymer Materials, Chair for Advanced Materials Synthesis, Institute for Functional Materials and Biofabrication, Department of Chemistry and Pharmacy, Julius-Maximilians-University Würzburg, Röntgenring 11, 97070 Würzburg, Germany*

[2]*Institute of Biomaterials, Friedrich Alexander University of Erlangen-Nürnberg, Cauerstr. 6, 91058, Erlangen, Germany*

[3]*Institute of Organic Chemistry, Julius-Maximilians-University Würzburg, Am Hubland, 97074 Würzburg, Germany*

[4]*Chair for X-Ray Microscopy, Julius-Maximilians-University Würzburg, Josef-Martin-Weg 63, 97074 Würzburg, Germany*

[5]*Department for Functional Materials in Medicine and Dentistry, Julius-Maximilians-University Würzburg, Pleicherwall 2, 97070 Würzburg, Germany*

[6]*Department of Chemistry, Johannes Gutenberg University Mainz, Duesbergweg 10-14, 55128 Mainz, Germany*

[7]*Soft Matter Chemistry, Department of Chemistry and Helsinki Institute of Sustainability Science, Faculty of Science, University of Helsinki, 00014 Helsinki, Finland*

Correspondence to: robert.luxenhofer@helsinki.fi

Keywords inverse gelation, aromatic moieties, 3D printing, bioink, shear-thinning

Abstract

Hydrogels are key components in several biomedical research areas such as drug delivery, tissue engineering and biofabrication. Here, a novel ABA-type triblock copolymer comprising poly(2-methyl-2-oxazoline) as the hydrophilic A blocks and poly(2-phenethyl-2-oxazoline) as the aromatic and hydrophobic B blocks is introduced. Above the critical micelle concentration, the polymer self assembles into small polymer micelles with a hydrodynamic radius of approx. 8 nm. Interestingly, this specific combination of hydrophilic and hydrophobic aromatic moieties leads to rapid thermoresponsive inverse gelation at polymer concentrations above a critical gelation concentration (20 wt.%) into a macroporous hydrogel. This hydrogel exhibited pronounced viscoelastic solid-like properties, as well as extensive shear thinning, rapid structure recovery and good strain resistance properties. Excellent 3D-printability of the cytocompatible hydrogel at lower temperature opens wide range of different applications, for example in the field of biofabrication. In preliminary bioprinting experiments using NIH 3T3 cells, excellent cell viabilities of more than 95 % were achieved. The particularly interesting feature of this novel material is that it can be used as printing support in hybrid bioink systems and sacrificial bioink due to rapid dissolution at physiological conditions.

Introduction

Thermosensitive water-soluble polymers undergo phase separation with respect to their physico-chemical properties due to small temperature changes. Phase separation upon heating is characterized by a lower critical solution temperature (LCST).[1] In contrast, in a polymer, which exhibits an upper critical solution temperature (UCST), phase separation, takes place upon cooling.[2-7] Exemplarily, Seuring et al. reported and characterized the UCST type phase separation properties of a nonionic homopolymer poly(*N*-acryloyl glycinamide) in pure water.[8] In a more recent study poly(acrylic acid) was copolymerized with acrylonitrile resulting in a UCST type copolymer combining the driving forces of hydrogen bonding and hydrophobic interactions.[9] In some rare cases hydrogel formation instead of phase separation/precipitation is observed. Over the last decades, most described systems in literature are based on synthetic or natural water-soluble polymers exhibiting lower critical solution temperature (LCST)-type thermosensitive gelation.[10-15] By introducing thermoresponsive units into the polymer structure, gelation can be induced at room or elevated temperatures as was described several times.[16, 17] Only a few examples can be found in literature were the gelation occurred via cooling the sample below a critical temperature (inverse gelation). Particularly prominent examples are natural biopolymers like gelatin and pectin/chitosan-systems.[18, 19] In 1998 Yoshioka et al. reported a gelatin-*g*-poly(*N*-isopropylacrylamide) graft copolymer which undergoes thermo- (above 34 °C) and inverse thermos (below 10 °C) gelation at 5 wt.%.[20] In addition to rheological investigations, the hypothetical use of this system in smart 3D cell-culture was discussed. In 2016 an inverse thermogelling system comprising a poly(poly(ethylene glycol) methyl ether methacrylate) middle block and a thermosensitive poly(acrylamide-*co*-acrylonitrile) (P(AAm-*co*-AN)) outer blocks was described.[21] The temperature dependent sol/gel properties were investigated in the temperature range of 8 °C to 80 °C and low polymer concentrations of 3 and 5 wt.%. At 8 °C a clear hydrogel was obtained. The sol/gel transition could be modulated by the polymer composition. By modifying a high molecular weight precursor copolymer comprising *N*,*N*-dimethylacrylamide and acrylic acid with hydrophobic moieties of *n*-dodecyl amine an inverse thermogelling hydrogel could be realized.[22] At 0 °C, a viscosity of ca. 1 kPa*s could be obtained by varying the sol/gel temperature with different polymer concentrations. However, no defined application as biomaterial has been described here either. Inspired by the water transfer of natural Mimosa, Chen and co-workers established a thermoresponsive bilayer

system in 2018.[23] One part of the system was an inverse thermogelling hydrogel formed by poly(acrylic acid-*co*-acrylamide) (PAAc-*co*-PAAm) layer. The system was discussed as actuator for the fabrication of intelligent soft materials for bio-inspired applications. Nevertheless, the embedding of living cells seems to be challenging as the cells sediment before polymerization and the actual hydrogel formation is performed at 50 °C under ultraviolet light (UV) exposure. The combination of such conditions can be expected to cause significant cytotoxicity. In 2019 Hua et al. reported a multi-thermoresponsive hydrogel system, which offers the possibility of 3D shape transition upon cooling in water and oil systems.[24] In the last years the interest in biofabrication, especially for tissue engineering and regenerative medicine has been rapidly growing into a promising interdisciplinary research field in its own right.[25] One major additive manufacturing technique used in the field is extrusion printing of bioinks.[26] Often a hydrogel formulation, which enables printability and cell survival during the printing process, is preferentially used.[27] To date, most commonly hydrogels based on natural biopolymers, such as gelatin, alginate and hyaluronic acid are used due to their generally good cytocompatibility.[28] However, such systems based on biopolymers can also have limitations such as less-than-ideal printability and often considerable batch-to-batch variations, especially with respect to rheological properties. The synthetic polymer platform formed by cyclic imino ethers, in particular poly(2-substituted-2-oxazoline)s (POx) and poly(2-substituted-5,6-dihydro-4H-1,3-oxazine)s (poly(2-oxazine)s, POzi), was investigated for decades as biomaterials in different applications due to good cytocompatibility and chemical versatility.[29-32] POx/POzi based systems were investigated as thermoresponsive materials[32], for biomedical applications[33, 34] and drug delivery[35] approaches. However, surprisingly few reports can be found that show thermogelation of pure POx/POzi polymers in water. In 2017 Lorson et al. established a thermogelling cytocompatible and printable supramolecular hydrogel based on POx/POzi diblock copolymers.[36] The system comprised a hydrophilic poly(2-methyl-2-oxazoline) (PMeOx) block and a thermoresponsive poly(2-*n*-propyl-2-oxazine) (P*n*PrOzi) block of similar block length. Another thermogelling hydrogel was described by Hoogenboom and Monnery.[37] A BAB triblock copolymer bearing poly(2-*n*-propyl-2-oxazoline) (P*n*PrOx) (B) and hydrophilic poly(2-ethyl-2-oxazoline) blocks (A) showed sol/gel transitions upon heating, but extremely high degrees of polymerization were required. In 2019, Lübtow, Mrlik *et al.* described a different, much shorter ABA triblock copolymer, which forms stable, but relatively weak and barely printable, thermogelling hydrogels.[38] Very recently, the first

inverse thermogelling hydrogel formed by POx/POzi based block copolymers was described. Here, the ABA triblock copolymer comprising the hydrophilic PMeOx (A) and the aromatic hydrophobic poly(2-phenyl-2-oxazine) (PPheOzi, B) blocks undergoes unique gelation at lower temperatures.[39] The stable hydrogel was formed by entangled self-assembled worm-like micelles, which form from spherical micelles upon cooling, leading to gelation. A potential application of such system as a biomaterial ink was mentioned. The limiting factor for using this system as a component in a bioink formulation is its gelation kinetics. Upon cooling, it takes about one hour to form a hydrogel suitable for printing, which is a rather long time if viable cells are to be embedded. Here, a new ABA triblock copolymer featuring the aromatic poly(2-phenethyl-2-oxazoline) (PPhenEtOx, B) is described, which undergoes inverse thermogelation in aqueous solution with pronounced and fast thermoresponsive sol/gel transition and characterized for further usage as a bioink component. The additional two CH_2-groups in the sidechain as well as the different backbone compared to the previously described inverse hydrogel platform, leads to higher structural flexibility and decreases the gelation time significantly, resulting in a new and unique gelation mechanism.

Experimental Section

In general, all substances and reagents for the monomer synthesis and polymerization were purchased from Sigma-Aldrich (Steinheim, Germany) and TCI-chemicals (Eschborn, Germany) and were used as received without further purification unless otherwise stated. For polymerization all substances were refluxed over CaH_2 for several hours and distilled prior usage. The solvent benzonitrile (PhCN) was dried over phosphorus pentoxide.

The monomer synthesis of 2-phenethyl-2-oxazoline (Scheme S1) was carried out as described by Wittig and Seeliger.[40] For the reaction 1 eq of 3-phenylpropionitrile, 1.2 eq of amino-ethanol and catalytic amounts of zinc acetate dihydrate were added to a argon flushed flask and heated to 130 °C under reflux for several days until the color of the reaction mixture turned brown. Reaction progress was controlled by ^{1}H NMR spectroscopy. After completion, the mixture was dissolved in dichloromethane and washed three times with H_2O. The organic phase was dried with $MgSO_4$ and concentrated. The raw product was refluxed with CaH_2 and purified via vacuum distillation under argon atmosphere yielding a colorless liquid. The resulting compound 2-phenethyl-2-oxazoline was characterized via refractive index, GC-ESI-MS analysis, and ^{1}H and ^{13}C NMR spectroscopy (See Supporting Information).

Refractive index measurements of the synthesized monomer 2-phenethyl-2-oxazoline was performed on a RFM 870 refractometer from Bellingham+Stanley at 20 °C (Farnborough, England).

The monomer was further analyzed via *mass-spectrometry* using an Agilent 5977B MDS system coupled with a gas-chromatography system Agilent 7820A. The GC-system was equipped with an Agilent 19091S-433UI HP-5ms ultra inert column (30 m x 250 µm x 0.25 µm). Temperature gradient was set from 40 °C to 300 °C with constant heat rate of 15 °C/min and a constant flow of 1 mL/min.

The ABA type copolymers were synthesized following a general procedure based on previous reports (detailed description in supporting information).[41, 42]

Nuclear magnetic resonance (NMR) was performed on a Bruker Fourier 300 (^{1}H: 300.12 MHz) spectrometer at 298 K from Bruker BioSpin (Rheinstetten, Germany) and calibrated using the residual protonated solvent signal.

Gel permeation chromatography (GPC) was performed on a Polymer Standard Service PSS (Mainz, Germany) system with following specifications: pump mod. 1260 infinity, MDS RI-detector mod. 1260 infinity (Agilent Technologies, Santa Clara, California, USA), precolumn: 50 x 8 mm PSS PFG linear M; 2 columns: 300 x 8 mm PSS PFG linear M (particle size 7 µm; pore size 0.1 – 1.000 kg/mol) with hexafluoroisopropanol (HFIP, containing 3 g/L potassium trifluoroacetate (KTFA)) as eluent calibrated against PEG standards with molar masses from 0.1 g/mol to 1000 kg/mol. The columns were held at 40 °C and the flow rate was set to 0.7 mL/min. Prior to each measurement, samples were dissolved in eluent and filtered through 0.2 µm PTFE filters (Rotilabo, Karlsruhe, Germany) to remove particles, if any.

Rolling ball viscosity experiments were performed on a LOVIS 2000M microviscometer from Anton Paar (Graz, Austria) using a LOVIS 1.8 capillary and a steel ball of 1.5 mm diameter. Prior to viscosity measurements the density was determined at 5 °C and 40 °C using a DMA 4100 M density meter from Anton Paar (Graz, Austria). A temperature scan from 5 °C → 40 °C and 40 °C → 5 °C of a 10, 15 and 20 wt.% aqueous sample was performed to establish the temperature dependent dynamic viscosity.

For *pyrene fluorescence assay* 40 µL pyrene solution (25 µM) in acetone were added to glass vials. The solvent was evaporated and 3 mL of polymer solutions of different concentrations in deionized water were added to yield final polymer concentrations of $1*10^{-7}$→$5*10^{-5}$ M and fixed pyrene concentration of $5*10^{-7}$ M. The pyrene fluorescence emission spectra ($\lambda_{exitation}$: 330 nm at 25 °C) were recorded on a FP-8300 spectrofluorometer system from Jasco (Gross-Umstadt, Germany) between 360→400 nm. To determine the critical micelle concentration, the I_1/I_3 ratios as a function of polymer concentration were fitted using Boltzmann fit function,

which is given by

$$y = \frac{A_1 - A_2}{1 + e^{(x-x_0)/\Delta x}} + A_2 \qquad (1)$$

with A_1 and A_2 are the upper and lower limits of the sigmoid, x_0 is the center of the sigmoid, and Δx is directly related to the range where the abrupt change of sigmoid occurs. The onset of abrupt decrease is defined as critical micelle concentration (CMC) and can be determined via equation 2, which is given by

$$x(CAC) = x_0 - 2\Delta x \qquad (2)$$

Rheology investigations were recorded on an Anton Paar (Ostfildern, Germany) Physica MCR 301 system utilizing a plate-plate geometry (25 mm diameter) equipped with a solvent trap and Peltier element for temperature control. All aqueous samples were measured after complete dissolution in Millipore water and a concentration of 20 wt.% at 5 °C. For investigations of viscoelastic behavior, the linear viscoelastic region (LVE) was determined by performing an amplitude sweep (0.02 %→500 %) strain deformation using a fixed angular frequency of 10 rad/s. Subsequently a frequency sweep (0.1 rad/s→100 rad/s) was performed at fixed strain deformation of 0.1 %. For dispense plotting rheological preconditions of the hydrogel are shear-thinning properties, defined force resistance profile and fast structure-recovery after deformation. For steady shear experiments, the control shear rate mode was used (0.001 1/s→1000 1/s). The pronounced viscosity η decrease was fitted using the power-law expression (eq. 3)

$$\eta = K \cdot (\dot{\gamma})^{n-1} \qquad (3)$$

Where K is the consistency index, n the flow index and $\dot{\gamma}$ the applied shear rate.

Using the steady stress sweep (5 Pa→1500 Pa) the onset value of viscosity decrease is refereed as yield point of the hydrogel system. To investigate the structure recovery properties, two different recovery testing experiments were performed. During the ORO-experiment (oscillation-rotational-oscillation) a low strain deformation of 0.5 % is followed by a high shear rate of 100 1/s. In ROR-experiment (rotational-oscillation-rotational) a low shear rate region of 0.1 1/s is followed by a high strain of 100 %.

Dynamic light scattering (DLS) experiments were performed on an ALV SP125 (Langen, Germany) equipped with a He-Ne-laser (22 mW, λ= 632.8 nm) and a single optical avalanche photodiode-detector. Scattering angles from 30→125 ° were measured with a 5 ° angle interval for aqueous samples and 30→70 ° for methanol samples (T = 293.15 K, correlation time 60s, average of 3-5 runs). Prior to each measurement, samples were dissolved in methanol (10 g/L) and filtered through 0.02 µm Anotop membrane filters from Whatman GE Healthcare followed by IC Millex-LG 0.2 µm. After evaporation of methanol the samples were dissolved in prefiltered (Millex-LG 0.2 µm) Millipore water containing 2 mM $NaNO_3$ or methanol. 1 g/L samples were filtered (Millex-LG 0.2 µm) into dust free cuvettes under laminar flow. The decay of the electric field-time autocorrelation function (ACF) was fitted using biexponential fit functions (equation 4) with respect to polydispersities:

$$g_1(t) = a_1 \cdot e^{\left(-\frac{t}{\tau_1}\right)} + a_2 \cdot e^{\left(-\frac{t}{\tau_2}\right)} \qquad (4)$$

With the amplitudes a_i and the decay time $\tau_i = \frac{1}{q^2 \cdot D_i}$ (q being the absolute value of the scattering vector and D the translational diffusion coefficient which is indirect proportional to the hydrodynamic radius R_h (Stokes-Einstein equation 2):

$$R_h = \frac{k_B \cdot T}{6 \cdot \pi \cdot \eta \cdot D} \qquad (5)$$

With Boltzmann constant k_B and the viscosity of the solvent η.

For *transmission electron microscopy (TEM)* investigations the polymer was dissolved in ultra pure water to a final concentration of 20 g/L. For the negative stain method, 400 mesh copper-rhodium grids (maxtaform) with a homemade carbon layer were glow-discharged in air for 1.5 min at medium power in a Harrick PDC-002 plasma cleaner. The 20 g/L sample was diluted (1/125) and 8 µL were incubated on the grids for one minute before blotting (Whatman filter paper No 50). Subsequently, the grids were washed with water (3x) and with 2 % (w/v) uranyl acetate (3x). For imaging a single-tilt room temperature holder in an FEI Tecnai T12 Spirit transmission electron microscope equipped with a LaB_6 emitter at 120 kV was used. Images were recorded with an Eagle CCD camera under low-dose conditions. The micrographs were binned 2 times resulting in a pixel size of 4.4 Å/pix at specimen level.

The temperature dependent ^1H NMR analysis was performed at a Bruker Avance III HD 600 spectrometer (Karlsruhe, Germany) operating at 600.4 MHz with a BBFO 5 mm probe. ^{1}H NMR experiments at different temperatures (5-40 °C) of a 20 wt.% hydrogel sample in D_2O/H_2O (1:1) were performed without sample spinning and 16 scans. The sample was kept for 10 minutes at the desired temperature prior to each measurement. Temperature calibration was done using 4 % MeOH in MeOD and 80 % ethylene glycol in DMSO-d_6. All recorded spectra were referenced using the temperature dependent HDO signal. For a more quantitative characterization of the temperature induced phase transition the fraction p was calculated with the integrals *I(T)* and *$I(T_0)$* at the respective temperatures T and T_0 using the following equation[43]:

$$p = 1 - \frac{I(T)}{I(T_0) * \frac{T_0}{T}} \qquad (6)$$

The highest signal intensity was measured at 40°C, which was chosen to be T_0. Reductions of signal intensity caused by inhibited molecular mobility due to gelation were quantified by values of $p < 0$.

For *small-angle (SAXS)* experiments an in-house setup at the Chair of X-ray microscopy at the University of Würzburg was used, which was built by Fraunhofer EZRT (Fürth, Germany). It consists of a MicroMax-007 HF X-ray source (Rigaku, Japan) and an Eiger R 1M detector unit (Dectris, Switzerland). The sample-detector distance can be varied between 5 cm and 3.5 m, which corresponds to possible Q-values between 0.005 and 5 $Å^{-1}$. The complete setup is operated in a vacuum below 0.1 mbar to reduce air scattering. The sample solutions (10 and 20 wt.%) were placed in quartz capillaries (inner diameter: 1 mm, wall thickness: 10 µm) (Hampton Research, Aliso Viejo, California), which were positioned perpendicularly to the X-ray beam. The presented experiments were done at sample-detector distances of 57 mm, 565 mm and 1560 mm with an integration time of 15 minutes for the shortest distance and 240 minutes for the two longer configurations. All distances were calibrated using a silver behenate standard sample. For each sample, data was acquired for different temperatures between 5-60 °C. To achieve thermal equilibrium, the sample was kept at the desired temperature for 15 minutes prior to each measurement. The SAXS data, which was obtained at the two largest distances, was calibrated in terms of absolute intensities using glassy carbon as a secondary calibration standard.[44, 45] The scattering curves of the hydrogels were obtained by azimuthal integration and corrections taking the samples thickness, X-ray transmission, detector accuracy, setup geometry and solvent scattering into account following the standard procedures described in literature.[46]

For *scanning electron microscopy* of the native hydrogel structure, we investigated a cryogenic sample preparation procedure. For this, hydrogel samples were placed between two aluminium holders (d=3mm), both containing a notch with a diameter of 2 mm, inclosing the sample and rapidly frozen in slush nitrogen (SN) at -210 °C. The samples were then transferred into the sputter coater with a Leica EM VCT100 cryo-shuttle at -140°C (Leica Microsystems ACE 400, Wetzlar, Germany). Here, the upper half of the sample was knocked off to create a fresh fractured surface and freeze-etched at -85 °C for 15 minutes under vacuum (< $1 \cdot 10^{-3}$ mbar). The samples were finally sputtered with 3 nm platinum and transferred with the cryo-shuttle into the SEM chamber. The morphology of the fractured surfaces was imaged at -140 °C, by detecting SE using acceleration voltages of 2 kV or 8 kV.

To investigate the *printability* of 20 wt.% hydrogel samples a compact bench-top 3D bioprinter (BioX, Cellink, Schweden) working on the principle of an extrusion-based technology was used. The printhead and the print bed were cooled to 8 °C prior to each fabrication process. The printing speed was set to 10 mm/s and a pressure of 120-160 kPa was applied (Nozzle: 25 G, stainless steel, length of 6.35 mm). First the printing resolution was investigated by increasing the strand-center to strand-center distance stepwise from 0.5 mm→0.75 mm→1 mm→1.5 mm→ 2 mm (Layer height 0.25 mm). To investigate the steadiness of the hydrogel a strand collapse test was investigated like described by Ribeiro et al.[47] The distance between the two edition points increased from 0.1→0.2→0.4→0.9→1.7 cm. Finally, real 3D- printing was performed by printing a 20 layered tubular construct of 5 mm total height and 5 mm diameter using the parameters already described.

To evaluate the *cytocompatibility* of POx/Alginate (20:1 wt.%) bioinks, the viability of NIH3T3 cells (ATCC, Germany, 1 Mio/mL) were embedded into the bioink. As a reference sodium alginate (VIVA Pharm, PH176, 1 wt.%) was used. After homogenous cell distribution at 37 °C a simple one layered square structure (Figure S6) was printed at 10 °C and printing pressure of 50 kPa and printing speed of 5 mm/s. Stabilization after printing was performed using a 0.1 M $CaCl_2$ aqueous solution (10 minutes). The crosslinked scaffolds were incubated for 24 h at 37 °C in cell culture medium (DMEM high glucose (Gibco from Sigma Aldrich) supplemented with 1% pen/strep, 2% glutamine (Thermo Fisher) and 10% bovine calf serum from Corning under controlled conditions (5% CO_2, 95% relative humidity). To assess the cell viability, printed NIH3T3-cells were stained insight the scaffolds using Calcein AM (Invitrogen, Thermo Fisher) after 24h of cultivation, whereas blue nuclei acid stain (DAPI) (Thermo Fisher) was used to visualize nuclei of all embedded cells. ImageJ software was used to determine the cell viability using automatic cell counting in 3 fluorescence images (n=3) of 3 different samples (n=3) obtained with an epifluorescence microscope (Zeiss Observer, Germany) using the following equation:

$$cell\ viability = \frac{[number\ of\ living\ cells]}{[number\ of\ cell\ nuclei]} \qquad (7)$$

Results and Discussion

Two batches of an ABA-triblock copolymer $PMeOx_{35}$-*b*-$PPhenEtOx_{15}$-*b*-$PMeOx_{35}$ (=A-PPhenEtOx-A) were synthesized by living cationic ring opening polymerization (LCROP) and characterized by ^{1}H NMR spectroscopy (Figure S2 and S5) and GPC (Figure S1 and S4). The successful termination using different terminating agents (P1: BOC-Pip, P2: EIP), the comparable degree of polymerization of approx. 90 repeating units as well as a ratio of PMeOx/PPhenEtOx of 4 was verified by corresponding signal intensities in ^{1}H NMR spectra. Via GPC the number average molar mass M_n and the dispersity Đ (M_w/M_n) of both batches were compared after completion of every single block and purification of the final polymer product. Both batches show reasonably narrow molar mass size distributions (Đ(P1): 1.12, Đ(P2): 1.17) and an increase of the number average molar mass during the polymerization reaction, indicative of the living polymerization. The primary structural difference between these novel polymers in comparison to the previously described aromatic amphiphiles is one additional methylene groups in the sidechains of every repeat unit in the central B block, which leads to significantly altered physico-chemical properties. Very similar to previously described ABA type amphiphiles, the novel polymers form stable nanoscale micelles in aqueous solutions above the CMC.[41, 48, 49] The investigated A-PPhenEtOx-A polymer exhibited a rather low CMC of 0.3 µM as determined by pyrene fluorescence measurement in dependency of the polymer concentration (Figure 1 A,B). The hydrodynamic radius of these nanoscale aggregates was determined via DLS at different scattering angles (Figure 1 C, D). In the non-selective solvent methanol, the hydrodynamic radius of an individual polymer chain was determined as ca. 2.4 nm. In contrast, in the selective solvent water, the polymers self-assemble into micelles with a hydrodynamic radius of ca. 8 nm. The low dependence on the scattering angle (30→125 °) suggests spherical micelles of low polydispersity (Figure 1 D). The spherical morphology of micelles could be further corroborated by means of transmission electron microscopy (Figure 1 E).

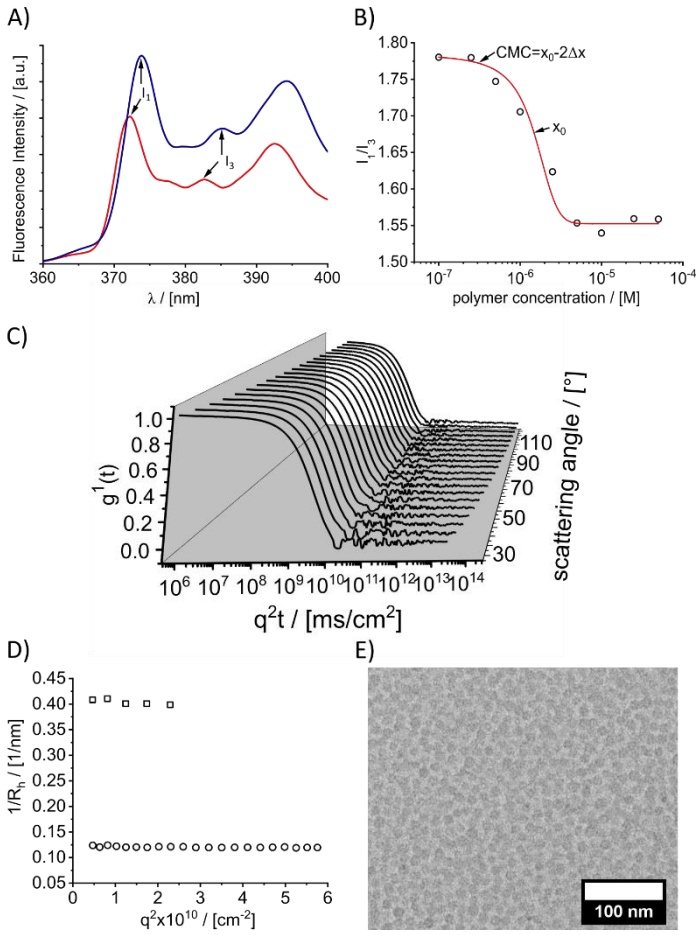

Figure 1| Self-assembly of A-PPhenEtOx-A at low polymer concentration in aqueous solution. A) Characteristic pyrene emission spectra at 25 °C and polymer concentrations of 10^{-7} M (red) and 10^{-5} M (blue). B) I_1/I_3 intensity ratio of pyrene signal at different polymer concentrations fitted with Boltzmann fit function (R^2:0.99707). C) Autocorrelation functions of DLS experiments of 1 g/L aqueous polymer solution containing 2 mM $NaNO_3$ at 20 °C and different scattering angles (30→125 ° in 5 ° steps). D) Inverse hydrodynamic radius in dependency of the scattering vector q^2 of 1 g/L aqueous polymer solution containing 2 mM $NaNO_3$ (○) compared to 1 g/L polymer solutions in methanol as non-selective solvent (□). E) TEM image from aqueous polymer solution stained with uranyl acetate visualizes spherical micelles.

Inspired by our previous finding for a similar ABA triblock,[39] we investigated the thermoresponsive properties. Indeed it was observed, that when the concentration exceeded 20 wt.%, a hydrogel was formed at low temperature (Figure 2A,B (P2), Figure S3 (P1)). However, investigating this phenomenon in more detail, crucial differences compared to the previously described material ($PMeOx_{35}$-*b*-$PPheOzi_{15}$-*b*-$PMeOx_{35}$) were found. The thermoresponsive behavior was evaluated by rolling ball viscosimetry at different concentrations (10, 15 and 20 wt.%) combined with a heating (5 °C→40 °C) and cooling (40 °C→5 °C) ramp. At 10 wt.% and 15 wt.%, the viscosity decreases steadily with increasing temperature ($\eta_{5°C}$(10 wt.%)= 9 mPa*s→ $\eta_{40°C}$(10 wt.%)= 3 mPa*s, $\eta_{5°C}$(15 wt.%)= 50 mPa*s→

$\eta_{40°C}$(10 wt.%)= 11 mPa*s) without any notable features. The cooling and heating ramps yield very similar values. In contrast, at 20 wt.% the viscosity increases very fast below a critical temperature of ~ 22 °C eventually trapping the ball, whereupon no further values are obtained (Figure 2 C). Increasing the temperature, the polymer solution again flows freely forming a moderately viscous solution with dynamic viscosity values of ~ 70 mPa*s at 40 °C. A notable hysteresis of approximately 3 °C was observed in this experiment.

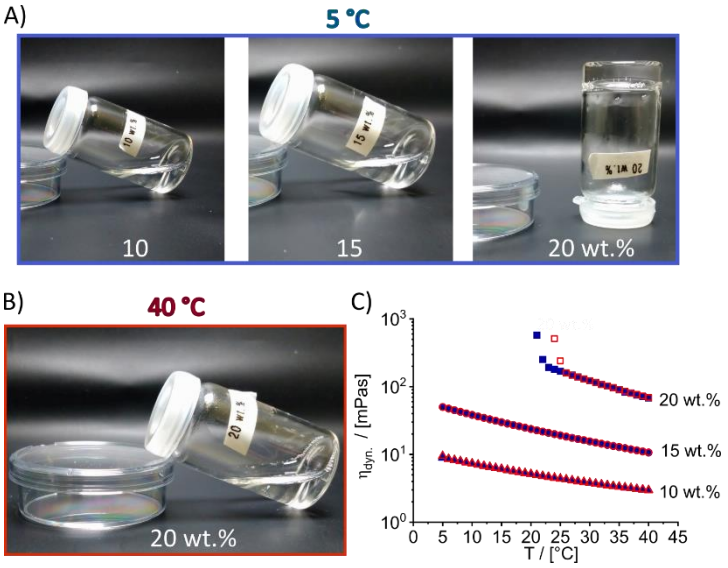

Figure 2| Increasing concentration of A-PPhenEtOx-A leads to hydrogel formation. A) Pictures of aqueous solutions at 5 °C and different polymer concentrations (10→15→20 wt.%). B) Picture of aqueous solution at 40 °C and a polymer concentration of 20 wt.%. C) Temperature dependent viscosity measurements (rolling ball system) at different polymer concentrations (blue and filled symbols: cooling, red and open symbols: heating).

To investigate the thermoresponsive aggregation on a molecular level, temperature dependent ^{1}H NMR experiments were conducted (Figure 3 A, B). At 5 °C, the signals attributed to the polymer backbone (3.45 ppm) and CH_3-sidechain (2.00 ppm) of the hydrophilic building blocks are visible, albeit broad and featureless. In the aromatic region (6.92 ppm) of the spectrum no signals are visible at 5 °C. That can be readily explained by very short transversal relaxation times T_2^* of the moieties in the hydrophobic micellar core, which are densely packed and apparently less hydrated so that efficient spin-spin relaxation can occur. As previously discussed, a gradual increase of the temperature from 5 to 40 °C causes liquefaction, and the signals of the hydrophilic as well as the hydrophobic part become narrower and more defined (Figure 3 A,B) as molecular mobility increases. Most interestingly, this is particularly visible in the aromatic region of the spectrum. An increasing, albeit still featureless signal is visible with increasing temperature, which is caused by more flexible units

of the hydrophobic core. Likewise, the reversibility of aggregation could be demonstrated by a subsequent cooling sequence, whereby the initial aggregation is achieved (Figure 4 B). A more quantitative insight was obtained by comparing the integrated NMR intensities of different polymer signals as a function of temperature (Figure 3C). A *p*-value (equation 6) of zero indicates the highest mobility in the liquid state (40 °C). The aromatic CH-protons are most strongly influenced yielding high *p*-values (close to 1= little signal intensity left) in the gel-state. Liquification due to increased temperature caused an increasing signal resulting in a steady *p*-value decrease up to 40 °C for the hydrophobic signals. The hydrophilic shell and the backbone are affected to a much lesser extent, similar to previous reports on the aggregation behavior of thermoresponsive phase separation of different POx based polymers.[43] In contrast to DLS, the polymer sol/gel could be investigated at concentrations needed for hydrogel formation (20 wt.%) using small angle X-ray scattering. At 5 °C, a significant structure peak was obtained (Figure 3 D). By increasing the temperature to 15 °C, the gel and micelle network become more mobile, which allows for a variation in the mean inter-micelle distance and leads to a shifting of the structure peak towards higher Q-values and a corresponding feature size of 17-18 nm hinting almost touching micelles (hydrodynamic diameter of 16 nm). By further increasing the temperature, the structure peak decreases, corroborating less correlation between the more mobile micellar structures in the sol-state. The fully reversibility of the aggregation was demonstrated by subsequently cooling to 5 °C after the first heating cycle (Figure 3 E). It appears at this point, that the hydrogel formation of A-PPhenEtOx-A is caused by densely packed spherical micelles, resembling the aggregation behavior of Pluronic F127. However, Pluronic F127 forms a hydrogel upon heating whereas PPhenEtOx-A does so upon cooling.

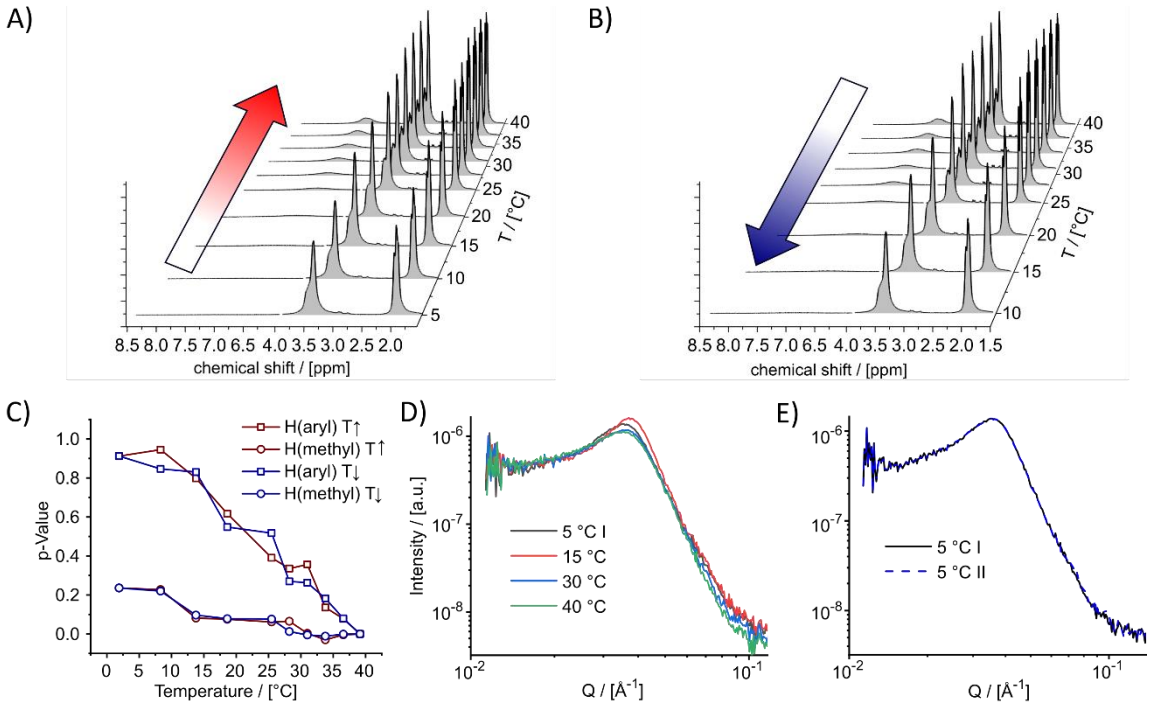

Figure 3| Temperature dependent aggregation by means of ^{1}H-NMR spectroscopy and SAXS experiments. ^{1}H-NMR spectra of a 20 wt.% hydrogel sample (H_2O/D_2O, 1:1) at different temperatures (A) 5 °C→40 °C, B) 40 °C→ 5 °C). C) p-Values for different polymer signals as a function of temperature. D) Small angle X-ray scattering of a 20 wt.% aqueous hydrogel sample at different temperatures (E: 5 °C, 15 °C, 30 °C and 40 °C). After the initial measurement, the sample was cooled again to 5 °C (E).

As previously mentioned, stimuli responsive hydrogels have been utilized in different biomaterials applications.[50] Recently, different approaches were established to overcome limitations in the so-called biofabrication window, especially in bioprinting.[51] One approach is to improve printability by support materials and sacrificial materials, while retaining cell viability utilizing biological components, cell-friendly crosslinking and mild printing conditions. The search for suitable hydrogel platforms is an ongoing challenge due to multiple specific and sometimes contradictive requirements. Appropriate gelation kinetics, good printability and cytocompatibility are key requirements for hydrogels during bioink design. Therefore, the viscoelastic properties of the present inverse thermogelling platform were thoroughly investigated via rheology. In the pronounced viscoelastic region (LVE, end of LVE marked with red line) a constant storage modulus G´ of 14.8±0.3 kPa was obtained with low damping factor of 0.3±0.02, which suggest a stable viscoelastic solid-like hydrogel (Figure 4 A). Interestingly, the hydrogel exhibits a profound dependency on the frequency (Figure 4 B). Increasing the frequency leads to increasing G´ and decreasing G`` values, i.e. the solid-like character is amplified with the dampening factor reaching values < 0.03 at 500 s^{-1}. To utilize a hydrogel as

3D-printable ink in different printing applications three major rheological considerations must be addressed, namely pronounced shear thinning, defined force resistance and fast structure recovery properties.[52] With increasing shear rate, the viscosity of the present hydrogel decreases following a power law expression with a flow index of 0.05±0.004, indicating very pronounced shear-thinning (Figure 4 C). Even at very low shear rates of 0.001 s^{-1}, no viscosity plateau is reached and shear stress values of ca. 200 Pa are measured at this point. In contrast, at very high shear rates of 1000 s^{-1} the viscosity values are very low (ca. 1 Pa*s) with shear stress values increasing up to 750 Pa. To obtain the yield point and the force resistance of the hydrogel, the viscosity was plotted as a function of the applied shear stress and split up in three regions (Figure 4D). Below the critical stress, almost constant viscosity values between 10^4 and 10^5 Pas with very low shear rates (between 10^{-4} and 10^{-5} 1/s) were determined (1.). At a certain stress, the viscosity decreases very fast with increasing shear rate values to low viscosity values (2.). The onset of 440 Pa is determined via two tangents. At high shear stress values of 800→1500 Pa a viscosity and shear rate plateau of 0.1 Pa*s and 10^3→10^4 s^{-1} are reached (3.). Structure recovery was tested using a 3 step test, designed as ORO (oscillation-rotational-oscillation) and ROR (rotational-oscillation-rotational) experiments, altering low and high strain regimes (Figure 4 E,F). In both cases, the structure recovered very fast and the initial values were obtained during the experiments, which we interpret to show rapid and complete structure recovery. To obtain insights into the hydrogel morphology, we conducted *cryogenic* scanning electron microscopy (*cryo*SEM) (Figure 4 G-I). A rather homogenous porous structure with pores in the range of several hundred nanometers was obtained. In comparison to a recently described hydrogel based on a A-PPheOzi-A triblock copolymer, the presently described A-PPhenEtOx-A hydrogel has significantly smaller pores.[39] In summary, the novel hydrogel shows promising viscoelastic characteristics for bioprinting.

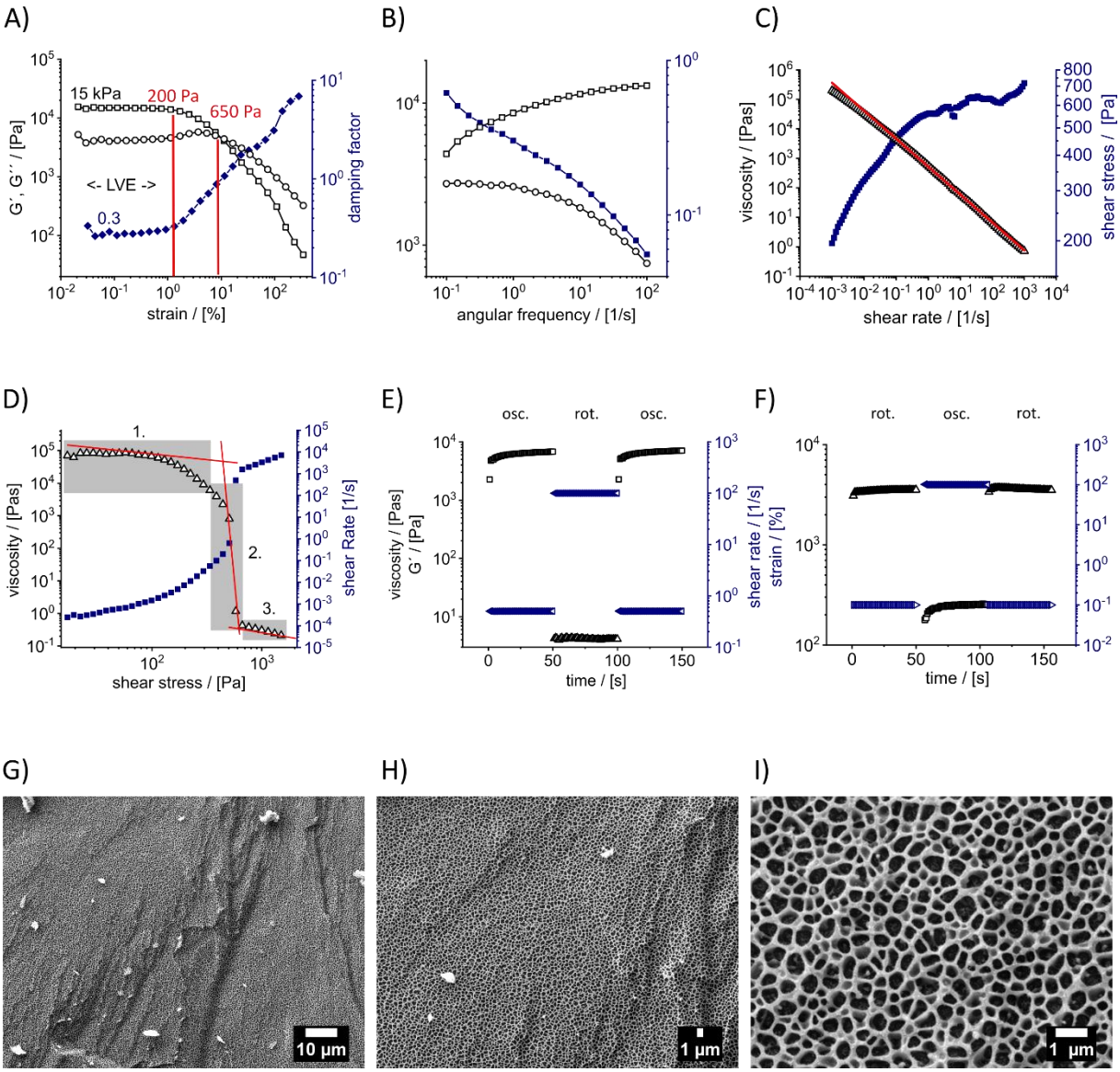

Figure 4| Rheological characterization for dispense plotting applications and cryoSEM analysis of A-PPhenEtOx-A hydrogel at 5 °C. A) Amplitude sweep of 20 wt.% hydrogel at 5 °C and an angular frequency of 10 rad/s with storage moduli (G´= □), loss moduli (G´´ = ○) and loss factor (■) shown. B) Frequency sweep with fixed amplitude of 0.1 %. C) Viscosity (Δ) and shear stress (■) in dependency of the applied shear rate for a 20 wt.% hydrogel. D) Viscosity (Δ) and shear rate (■) as a function of applied shear stress in steady shear stress experiment. E) ORO (oscillation-rotational-oscillation) recovery test of hydrogel. F) ROR (rotational-oscillation-rotational) 3 step recovery. G-I) *Cryo*-SEM images of 20 wt.% hydrogel at 1k x→2k x→10k x magnification.

Based on favorable rheological properties the printability of the hydrogel was investigated using extrusion-based printing (Figure 5 A-D). Additionally, a hybrid system comprising the POx based hydrogel and alginate was prepared, printed and stabilized with $CaCl_2$ (Figure 5 E-H). Alginate hydrogels are widely used in biofabrication as alginate is easily crosslinked by the addition of $CaCl_2$ after printing to stabilize the constructs. However, the printability of pure

sodium alginate without the addition of viscosity enhancers or modifications is very low.[53] First, we screened for the highest achievable resolution by printing hydrogel lines with decreasing line distance, from 2→1.5→1→0.75→0.5 mm (Figure 5 A, E). Even at a layer distance of 0.75 mm every individual strand could be distinguish and no strand fusion was observed. Additionally, the collapse of suspended filaments was investigated.[47] A free hanging hydrogel strut over a total distance of 1.7 cm could be realized without significant strand sag (Figure 5 B,F). Based on these promising results a first real 3D construct was printed (Figure 5 C,D,G,H Supporting Movie 1). A 20-layered cylindrical construct with a diameter of 5 mm and a total height of 5 mm was printed. The structure stayed intact, and no significant collapse was observed. The structure of the stabilized POx/alginate tubular construct was preserved even after 24h of incubation in PBS solution at 37 °C (Figure G, H).

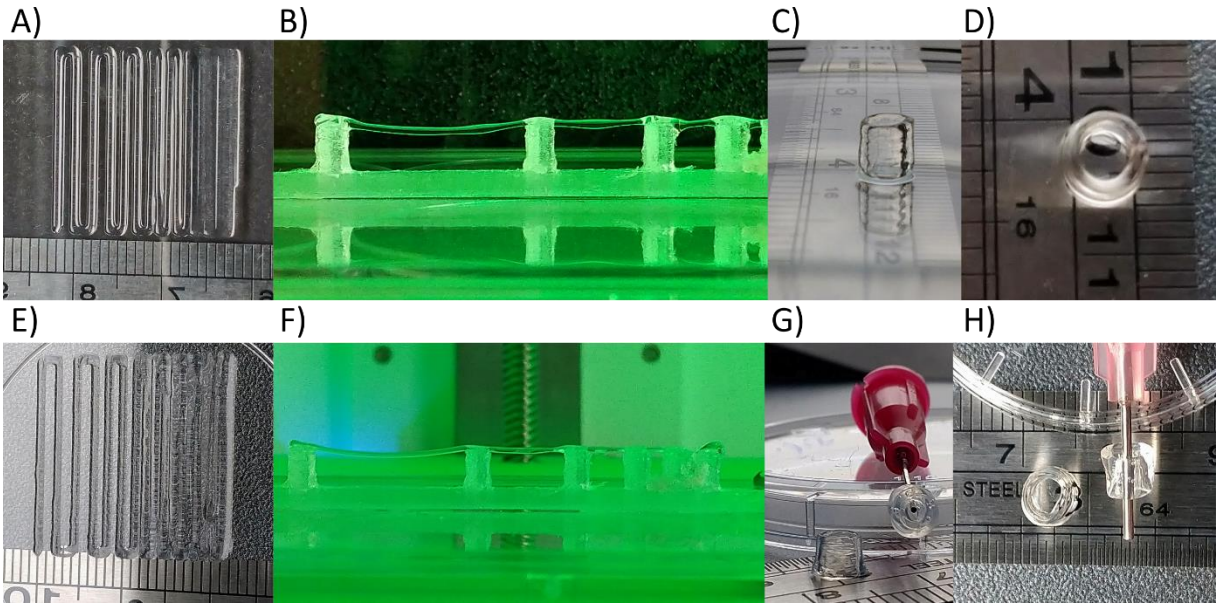

Figure 5| Extrusion printing of a A-PPhenEtOx-A 20 wt.% hydrogel (A-D) and a hybrid hydrogel of A-PPhenEtOx-A and alginate (E-H) at 8 °C (Nozzle 25 G, speed: 10 mm/s). A,E) Filament fusion test to visualize printing resolution. B,F) Filament collapse test by printing bridges of increasing distances. C,D,G,H) Printed 20 layer (5x5 mm cylindrical tube structures) constructs (top and side view).

Finally, a first bioprinting process was performed and the cytocompatibility was investigated using the POx/alginate (20:1 wt.%) hybrid system in comparison to pure alginate (1 wt.%) (Figure 6) after 24 h. After dissolving the polymers in cell culture medium, the cells were dispersed in the homogenous free flowing viscous liquid at 37 °C. The relatively high viscosity of the bioink precursor at 37 °C (see figure 2) prevented significant cell sedimentation. The bioink was transferred to the precooled bioprinter equipped with a cooling system. Using the

pronounced inverse gelation of A-PPhenEtOx-A as described above, cell laden constructs were obtained and stabilized via crosslinking of alginate using $CaCl_2$ aqueous solution. After 24h of incubation, cell staining was performed and quantified. Overall, the bioprinting process of POx based bioinks was found to be highly cytocompatible (cell viability > 95 %) and no significant difference with respect to cytocompatibility was observed for the hybrid formulation in comparison to alginate solution. However, in contrast to plain alginate, the hybrid system can be 3D printed with excellent shape fidelity.

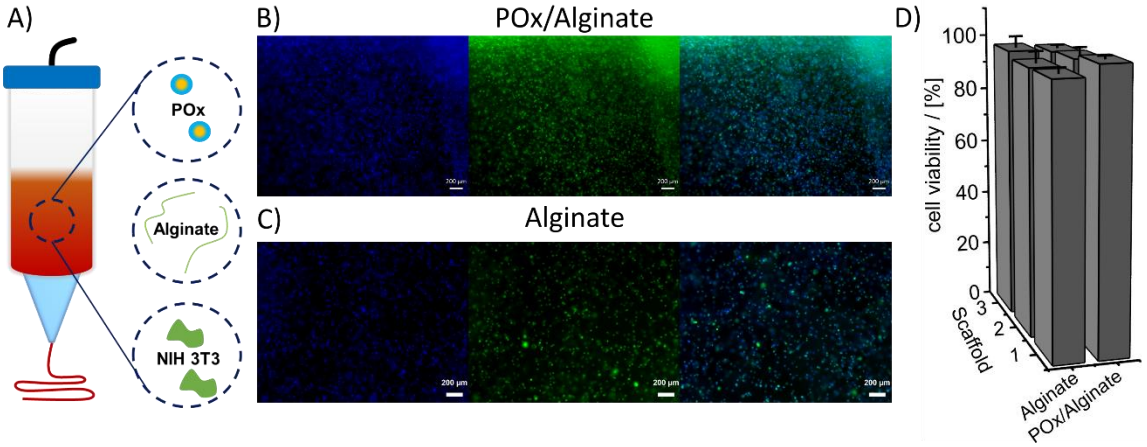

Figure 6| Cytocompatible bioprinting of POx/alginate based bioinks using NIH 3T3 cells (A). B), C) Single and merged fluorescence images of embedded NIH3T3-cells in POx/alginate (upper row) and alginate (bottom row) stained with DAPI (blue) and Calceine AM (green) after printing, stabilization with $CaCl_2$ and 24 h of incubation. D) Cell viability of NIH3T3-cells in 3 different printed scaffolds of alginate and POx/alginate hybrid formulation.

Conclusion:

Here, a new ABA type amphiphile based on poly(2-oxazoline)s with an aromatic hydrophobic central block of poly(2-phenethyl-2-oxazoline) B was described. Above the critical micelle concentration small spherical nanoscale micelles were confirmed. By increasing the concentration an inverse and fast sol/gel transition was observed due to densely packed micelles confirmed via temperature dependent ^1H NMR and SAXS experiments. Favorable rheological properties, such as pronounced viscoelastic solid-like properties, shear thinning, and structure recovery properties led to very good 3D printability of the investigated hydrogel. In a hybrid ink formulation comprising the readily printable POx based polymer and the biopolymer alginate, stable constructs were obtained. First cytocompatible bioprinting at approximately 10 °C for a A-PPhenOx-A/alginate hybrid system concluded the study and opens a wide range of different applications in the field of biofabrication.

Acknowledgement

The authors would like to gratefully acknowledge support by the Deutsche Forschungsgemeinschaft (DFG, German Research Foundation)-project number 326998133-TRR225 (subprojects A03, B06). Furthermore, we thank the Deutsche Forschungsgemeinschaft for funding the crossbeam scanning electron microscope Zeiss CB 340 (INST 105022/58-1 FUGG) within the DFG State Major Instrumentation Programm. We gratefully acknowledge access to electron microscopy facilities provided by Prof. Bettina Böttcher at the Rudolf Virchow Center, Julius-Maximilians-University Würzburg.

Supporting Information

Detailed description of monomer and polymer synthesis and characterization. Additional movie of extrusion printing process.

Notes:

LH and RL is listed as inventor on a patent pertinent to some materials in the present work. The authors declare no other competing financial interest.

References

1. Zhang, Q.; Weber, C.; Schubert, U. S.; Hoogenboom, R., Thermoresponsive Polymers with Lower Critical Solution Temperature: From Fundamental Aspects and Measuring Techniques to Recommended Turbidimetry Conditions. Materials Horizons 2017, 4 (2), 109-116.
2. Seuring, J.; Agarwal, S., Non-Ionic Homo- and Copolymers with H-Donor and H-Acceptor Units with an Ucst in Water. Macromolecular Chemistry and Physics 2010, 211 (19), 2109-2117.
3. Seuring, J.; Agarwal, S., Polymers with Upper Critical Solution Temperature in Aqueous Solution. 2012, 33 (22), 1898-1920.
4. Shimada, N.; Ino, H.; Maie, K.; Nakayama, M.; Kano, A.; Maruyama, A., Ureido-Derivatized Polymers Based on Both Poly(Allylurea) and Poly(L-Citrulline) Exhibit Ucst-Type Phase Transition Behavior under Physiologically Relevant Conditions. Biomacromolecules 2011, 12 (10), 3418-3422.
5. Meiswinkel, G.; Ritter, H., A New Type of Thermoresponsive Copolymer with Ucst-Type Transitions in Water: Poly(N-Vinylimidazole-Co-1-Vinyl-2-(Hydroxymethyl)Imidazole). 2013, 34 (12), 1026-1031.
6. Aseyev, V.; Tenhu, H.; Winnik, F., Non-Ionic Thermoresponsive Polymers in Water. 2010; Vol. 242, pp 29-89.
7. Niskanen, J.; Tenhu, H., How to Manipulate the Upper Critical Solution Temperature (Ucst)? Polymer Chemistry 2017, 8 (1), 220-232.
8. Seuring, J.; Bayer, F. M.; Huber, K.; Agarwal, S., Upper Critical Solution Temperature of Poly(N-Acryloyl Glycinamide) in Water: A Concealed Property. Macromolecules 2012, 45 (1), 374-384.
9. Zhao, C.; Dolmans, L.; Zhu, X. X., Thermoresponsive Behavior of Poly(Acrylic Acid-Co-Acrylonitrile) with a Ucst. Macromolecules 2019, 52 (12), 4441-4446.
10. Plunkett, K. N.; Zhu, X.; Moore, J. S.; Leckband, D. E., Pnipam Chain Collapse Depends on the Molecular Weight and Grafting Density. Langmuir 2006, 22 (9), 4259-4266.
11. Gupta, N. R.; Torris A. T, A.; Wadgaonkar, P. P.; Rajamohanan, P. R.; Ducouret, G.; Hourdet, D.; Creton, C.; Badiger, M. V., Synthesis and Characterization of Pepo Grafted Carboxymethyl Guar and Carboxymethyl Tamarind as New Thermo-Associating Polymers. Carbohydrate Polymers 2015, 117, 331-338.
12. Karakasyan, C.; Lack, S.; Brunel, F.; Maingault, P.; Hourdet, D., Synthesis and Rheological Properties of Responsive Thickeners Based on Polysaccharide Architectures. Biomacromolecules 2008, 9 (9), 2419-2429.
13. Bokias, G.; Mylonas, Y.; Staikos, G.; Bumbu, G. G.; Vasile, C., Synthesis and Aqueous Solution Properties of Novel Thermoresponsive Graft Copolymers Based on a Carboxymethylcellulose Backbone. Macromolecules 2001, 34 (14), 4958-4964.
14. Koonar, I.; Zhou, C.; Hillmyer, M. A.; Lodge, T. P.; Siegel, R. A., Abc Triblock Terpolymers Exhibiting Both Temperature- and Ph-Sensitive Micellar Aggregation and Gelation in Aqueous Solution. Langmuir 2012, 28 (51), 17785-17794.
15. Taribagil, R. R.; Hillmyer, M. A.; Lodge, T. P., Hydrogels from Aba and Abc Triblock Polymers. Macromolecules 2010, 43 (12), 5396-5404.
16. Niu, H.; Wang, F.; Weiss, R. A., Hydrophobic/Hydrophilic Triblock Copolymers: Synthesis and Properties of Physically Cross-Linked Hydrogels. Macromolecules 2015, 48 (3), 645-654.
17. Tuncaboylu, D. C.; Argun, A.; Sahin, M.; Sari, M.; Okay, O., Structure Optimization of Self-Healing Hydrogels Formed Via Hydrophobic Interactions. Polymer 2012, 53 (24), 5513-5522.
18. Djabourov, M.; Leblond, J.; Papon, P., Gelation of Aqueous Gelatin Solutions. Ii. Rheology of the Sol-Gel Transition. Journal de Physique 1988, 49 (2), 333-343.
19. Birch, N. P.; Barney, L. E.; Pandres, E.; Peyton, S. R.; Schiffman, J. D., Thermal-Responsive Behavior of a Cell Compatible Chitosan/Pectin Hydrogel. Biomacromolecules 2015, 16 (6), 1837-1843.
20. Yoshioka, H.; Mori, Y.; Tsukikawa, S.; Kubota, S., Thermoreversible Gelation on Cooling and on Heating of an Aqueous Gelatin–Poly(N-Isopropylacrylamide) Conjugate. 1998, 9 (2), 155-158.

21. Fu, W.; Zhao, B., Thermoreversible Physically Crosslinked Hydrogels from Ucst-Type Thermosensitive Aba Linear Triblock Copolymers. Polymer Chemistry 2016, 7 (45), 6980-6991.
22. Parmar, I. A.; Shedge, A. S.; Badiger, M. V.; Wadgaonkar, P. P.; Lele, A. K., Thermo-Reversible Sol–Gel Transition of Aqueous Solutions of Patchy Polymers. RSC Advances 2017, 7 (9), 5101-5110.
23. Zheng, J.; Xiao, P.; Le, X.; Lu, W.; Théato, P.; Ma, C.; Du, B.; Zhang, J.; Huang, Y.; Chen, T., Mimosa Inspired Bilayer Hydrogel Actuator Functioning in Multi-Environments. Journal of Materials Chemistry C 2018, 6 (6), 1320-1327.
24. Hua, L.; Xie, M.; Jian, Y.; Wu, B.; Chen, C.; Zhao, C., Multiple-Responsive and Amphibious Hydrogel Actuator Based on Asymmetric Ucst-Type Volume Phase Transition. ACS Applied Materials & Interfaces 2019, 11 (46), 43641-43648.
25. Groll, J.; et al., Biofabrication: Reappraising the Definition of an Evolving Field. Biofabrication 2016, 8 (1), 13001.
26. Groll, J.; Burdick, J. A.; Cho, D. W.; Derby, B.; Gelinsky, M.; Heilshorn, S. C.; Jüngst, T.; Malda, J.; Mironov, V. A.; Nakayama, K.; Ovsianikov, A.; Sun, W.; Takeuchi, S.; Yoo, J. J.; Woodfield, T. B. F., A Definition of Bioinks and Their Distinction from Biomaterial Inks. Biofabrication 2018, 11 (1), 013001.
27. Chimene, D.; Kaunas, R.; Gaharwar, A. K., Hydrogel Bioink Reinforcement for Additive Manufacturing: A Focused Review of Emerging Strategies. 2020, 32 (1), 1902026.
28. Valot, L.; Martinez, J.; Mehdi, A.; Subra, G., Chemical Insights into Bioinks for 3d Printing. Chemical Society Reviews 2019, 48 (15), 4049-4086.
29. Glassner, M.; Vergaelen, M.; Hoogenboom, R., Poly(2-Oxazoline)S: A Comprehensive Overview of Polymer Structures and Their Physical Properties. Polymer International 2018, 67 (1), 32-45.
30. Lorson, T.; Lübtow, M. M.; Wegener, E.; Haider, M. S.; Borova, S.; Nahm, D.; Jordan, R.; Sokolski-Papkov, M.; Kabanov, A. V.; Luxenhofer, R., Poly(2-Oxazoline)S Based Biomaterials: A Comprehensive and Critical Update. Biomaterials 2018, 178, 204-280.
31. Luxenhofer, R.; Jordan, R., Poly(2-Oxazoline)S (Pox) in Biomedical Applications. 2013; Vol. 8, p 70-73.
32. Dargaville, T. R.; Park, J. R.; Hoogenboom, R., Poly(2-Oxazoline) Hydrogels: State-of-the-Art and Emerging Applications. Macromol Biosci 2018, 18 (6), e1800070.
33. Harris, J. M.; Bentley, M. D.; Moreadith, R. W.; Viegas, T. X.; Fang, Z.; Yoon, K.; Weimer, R.; Dizman, B.; Nordstierna, L., Tuning Drug Release from Polyoxazoline-Drug Conjugates. European Polymer Journal 2019, 120, 109241.
34. Moreadith, R. W.; Viegas, T. X.; Bentley, M. D.; Harris, J. M.; Fang, Z.; Yoon, K.; Dizman, B.; Weimer, R.; Rae, B. P.; Li, X.; Rader, C.; Standaert, D.; Olanow, W., Clinical Development of a Poly(2-Oxazoline) (Poz) Polymer Therapeutic for the Treatment of Parkinson's Disease – Proof of Concept of Poz as a Versatile Polymer Platform for Drug Development in Multiple Therapeutic Indications. European Polymer Journal 2017, 88, 524-552.
35. Sedlacek, O.; Hoogenboom, R., Drug Delivery Systems Based on Poly(2-Oxazoline)S and Poly(2-Oxazine)S. 2020, 3 (1), 1900168.
36. Lorson, T.; Jaksch, S.; Lubtow, M. M.; Jungst, T.; Groll, J.; Luhmann, T.; Luxenhofer, R., A Thermogelling Supramolecular Hydrogel with Sponge-Like Morphology as a Cytocompatible Bioink. Biomacromolecules 2017, 18 (7), 2161-2171.
37. Monnery, B. D.; Hoogenboom, R., Thermoresponsive Hydrogels Formed by Poly(2-Oxazoline) Triblock Copolymers. Polymer Chemistry 2019, 10 (25), 3480-3487.
38. Lübtow, M. M.; Mrlik, M.; Hahn, L.; Altmann, A.; Beudert, M.; Lühmann, T.; Luxenhofer, R., Temperature-Dependent Rheological and Viscoelastic Investigation of a Poly(2-Methyl-2-Oxazoline)-B-Poly(2-Iso-Butyl-2-Oxazoline)-B-Poly(2-Methyl-2-Oxazoline)-Based Thermogelling Hydrogel. 2019, 10 (3), 36.
39. Hahn, L.; Maier, M.; Stahlhut, P.; Beudert, M.; Flegler, V.; Forster, S.; Altmann, A.; Toppke, F.; Fischer, K.; Seiffert, S.; Bottcher, B.; Luhmann, T.; Luxenhofer, R., Inverse Thermogelation of

Aqueous Triblock Copolymer Solutions into Macroporous Shear-Thinning 3d Printable Inks. ACS Appl Mater Interfaces 2020, 12 (11), 12445-12456.
40. Witte, H.; Seeliger, W., Simple Synthesis of 2-Substituted 2-Oxazolines and 5,6-Dihydro-4h-1,3-Oxazines. Angewandte Chemie International Edition in English 1972, 11 (4), 287-288.
41. Hahn, L.; Lübtow, M. M.; Lorson, T.; Schmitt, F.; Appelt-Menzel, A.; Schobert, R.; Luxenhofer, R., Investigating the Influence of Aromatic Moieties on the Formulation of Hydrophobic Natural Products and Drugs in Poly(2-Oxazoline)-Based Amphiphiles. Biomacromolecules 2018, 19 (7), 3119-3128.
42. Lübtow, M. M.; Hahn, L.; Haider, M. S.; Luxenhofer, R., Drug Specificity, Synergy and Antagonism in Ultrahigh Capacity Poly(2-Oxazoline)/Poly(2-Oxazine) Based Formulations. Journal of the American Chemical Society 2017, 139 (32), 10980-10983.
43. Konefał, R.; Spěváček, J.; Černoch, P., Thermoresponsive Poly(2-Oxazoline) Homopolymers and Copolymers in Aqueous Solutions Studied by Nmr Spectroscopy and Dynamic Light Scattering. European Polymer Journal 2018, 100, 241-252.
44. Dreiss, C. A.; Jack, K. S.; Parker, A. P., On the Absolute Calibration of Bench-Top Small-Angle X-Ray Scattering Instruments: A Comparison of Different Standard Methods. Journal of Applied Crystallography 2006, 39 (1), 32-38.
45. Zhang, F.; Ilavsky, J.; Long, G. G.; Quintana, J. P. G.; Allen, A. J.; Jemian, P. R., Glassy Carbon as an Absolute Intensity Calibration Standard for Small-Angle Scattering. Metallurgical and Materials Transactions A 2010, 41 (5), 1151-1158.
46. Pauw, B. R.; Smith, A. J.; Snow, T.; Terrill, N. J.; Thunemann, A. F., The Modular Small-Angle X-Ray Scattering Data Correction Sequence. Journal of Applied Crystallography 2017, 50 (6), 1800-1811.
47. Ribeiro, A.; Blokzijl, M. M.; Levato, R.; Visser, C. W.; Castilho, M.; Hennink, W. E.; Vermonden, T.; Malda, J., Assessing Bioink Shape Fidelity to Aid Material Development in 3d Bioprinting. Biofabrication 2017, 10 (1), 014102.
48. Luxenhofer, R.; Schulz, A.; Roques, C.; Li, S.; Bronich, T. K.; Batrakova, E. V.; Jordan, R.; Kabanov, A. V., Doubly Amphiphilic Poly(2-Oxazoline)S as High-Capacity Delivery Systems for Hydrophobic Drugs. Biomaterials 2010, 31 (18), 4972-4979.
49. Seo, Y.; Schulz, A.; Han, Y.; He, Z.; Bludau, H.; Wan, X.; Tong, J.; Bronich, T. K.; Sokolsky, M.; Luxenhofer, R.; Jordan, R.; Kabanov, A. V., Poly(2-Oxazoline) Block Copolymer Based Formulations of Taxanes: Effect of Copolymer and Drug Structure, Concentration, and Environmental Factors. Polymers for Advanced Technologies 2015, 26 (7), 837-850.
50. Sood, N.; Bhardwaj, A.; Mehta, S.; Mehta, A., Stimuli-Responsive Hydrogels in Drug Delivery and Tissue Engineering. Drug Delivery 2016, 23 (3), 748-770.
51. Malda, J.; Visser, J.; Melchels, F. P.; Jüngst, T.; Hennink, W. E.; Dhert, W. J. A.; Groll, J.; Hutmacher, D. W., 25th Anniversary Article: Engineering Hydrogels for Biofabrication. Advanced Materials 2013, 25 (36), 5011-5028.
52. Naomi, P.; Willi, S.; Thomas, B.; Ferry, M.; Jürgen, G.; Tomasz, J., Proposal to Assess Printability of Bioinks for Extrusion-Based Bioprinting and Evaluation of Rheological Properties Governing Bioprintability. Biofabrication 2017, 9 (4), 044107.
53. Hazur, J.; Detsch, R.; Karakaya, E.; Kaschta, J.; Teßmar, J.; Schneidereit, D.; Friedrich, O.; Schubert, D. W.; Boccaccini, A. R., Improving Alginate Printability for Biofabrication: Establishment of a Universal and Homogeneous Pre-Crosslinking Technique. Biofabrication 2020, 12 (4), 045004.